

# Strain and onsite-correlation tunable quantum anomalous Hall phases in ferromagnetic (111) $\text{LaXO}_3$ bilayers ( $\text{X}=\text{Pd}, \text{Pt}$ )

Hai-Shuang Lu<sup>1,2</sup> and Guang-Yu Guo<sup>1,3,\*</sup>

<sup>1</sup>*Department of Physics and Center for Theoretical Sciences,  
National Taiwan University, Taipei 10617, Taiwan*

<sup>2</sup>*College of Physics and Electronic Engineering, Changshu Institute of Technology, Changshu 215500, P. R. China*

<sup>3</sup>*Physics Division, National Center for Theoretical Sciences, Hsinchu 30013, Taiwan*

(Dated: December 25, 2021)

Quantum anomalous Hall (QAH) phases in magnetic topological insulators are characterized by the scattering-free chiral edge currents protected by their nontrivial bulk band topology. To fully explore these intriguing phenomena and application of topological insulators, high temperature material realization of QAH phases is crucial. In this paper, based on extensive first-principles density functional theory calculations, we predict that perovskite bilayers  $(\text{LaXO}_3)_2$  ( $\text{X} = \text{Pd}, \text{Pt}$ ) imbedded in the (111)  $(\text{LaXO}_3)_2/(\text{LaAlO}_3)_{10}$  superlattices are high Curie temperature ferromagnets that host both QAH and Dirac semimetal phases, depending on the biaxial strain and onsite electron correlation. In particular, both the direction (the sign of Chern number) and spin-polarization of the chiral edge currents are tunable by either onsite electron correlation or biaxial in-plane strain. Furthermore, the nontrivial band gap can be enhanced up to 92 meV in the  $\text{LaPdO}_3$  bilayer by the compressive in-plane strain, and can go up to as large as 242 meV when the Pd atoms are replaced by the heavier Pt atoms. Finally, the microscopic mechanisms of the ferromagnetic coupling and other interesting properties of the bilayers are uncovered by analyzing their underlying electronic band structures.

## I. INTRODUCTION

In the past decade, various topological insulators [1–3] have attracted enormous attention because of their fascinating transport properties. In particular, transport currents along the gapless edge modes on the surface or at the interface between two topologically different insulators are unidirectional and robust against scattering from disorder due to topologically nontrivial properties of their bulk band structures. The quantum anomalous Hall (QAH) phase, first proposed by Haldane in his Nobel Prize-winning paper [4], is a two-dimensional (2D) bulk ferromagnetic (FM) topological insulator (Chern insulator) with a nonzero topological invariant known as the Chern number in the presence of spin-orbit coupling (SOC) but in the absence of applied magnetic fields [3]. Its associated chiral edge modes carry dissipationless unidirectional electrical current. Due to the intriguing nontrivial topological properties and fascinating potential application for designing low energy consumption electronics and spintronics, extensive theoretical studies have been made recently to search for real QAH insulators [3]. Indeed, specific material systems such as FM quantum wells [5], FM topological insulator (TI) films [6], graphene on magnetic substrates [7, 8], and noncoplanar antiferromagnetic (AF) layered oxide [9] have been predicted.

Excitingly, this intriguing QAH phase was recently observed in the Cr-doped  $(\text{Bi,Sb})_2\text{Te}_3$  films [10]. However, the QAH phase occurs only at very low temperatures due

to the small band gap, weak magnetic coupling and low carrier mobility in the sample. This hampers further exploration of the novel properties of Chern insulators and also their applications. The low carrier mobility could result from the disorder due to the doped magnetic impurities in the sample, while the weak magnetic coupling could originate from the localized Cr 3d orbitals which hardly overlap with the orbitals of the neighboring Cr atoms. The problems of the weak magnetic coupling and small band gap could be overcome by introducing 4d and 5d transition metal atoms which simultaneously have more extended d orbitals and stronger SOC. Clearly, it would be fruitful to search for high temperature QAH phase in stoichiometry FM 4d and 5d transition metal compounds.

Transition metal oxides (TMOs) cover a wide range of crystalline structures and exhibit a rich variety of fascinating properties such as charge-orbital ordering, high temperature superconductivity, colossal magnetoresistance and half-metallic behavior [11]. Artificial atomic scale TMO heterostructures offer the prospect of further enhancing these fascinating properties or of combining them to realize novel properties and functionalities [12, 13] such as the conductive interface between two insulating oxides [14–16]. Recently, based on their tight-binding (TB) modelling and first-principles density functional theory (DFT) calculations, Xiao *et al.* proposed in their seminal paper [17] that various quantum topological phases could be found in a class of (111) TMO perovskite bilayers sandwiched by insulating perovskites where the transition metal atoms in the bilayers form a buckled honeycomb lattice which is known to host such topological phases as QAH phase [4]. Subsequently, the electronic structure of a large number of (111) TMO per-

---

\*Electronic address: gyguo@phys.ntu.edu.tw

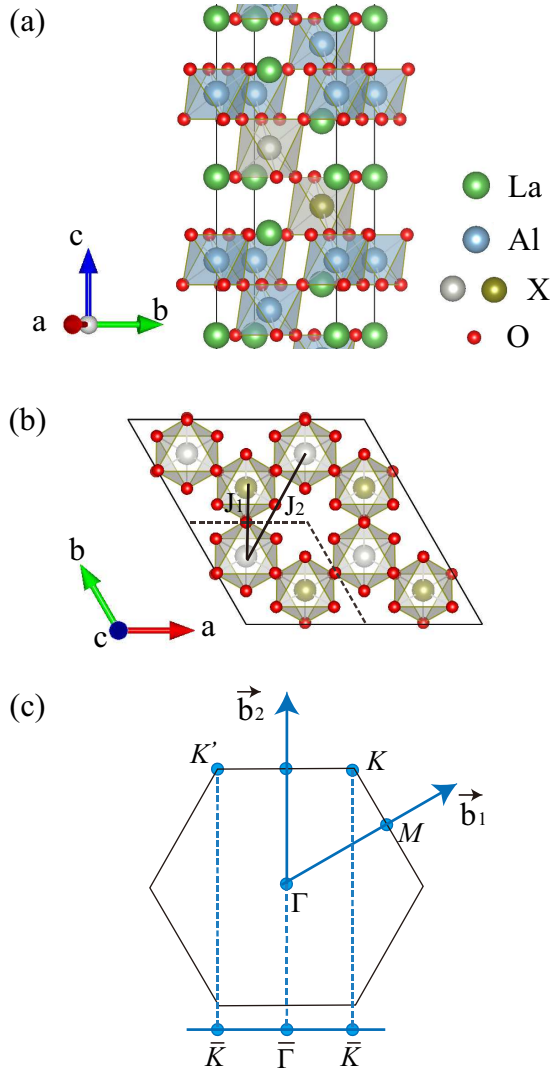


FIG. 1: Crystal structure of a  $(\text{LaXO}_3)_2/(\text{LaAlO}_3)_{10}$  superlattice. (a) Side view of the unit cell containing the  $(\text{LaXO}_3)_2$  bilayer, and (b) Top view of the  $(\text{LaXO}_3)_2$  bilayer forming a buckled honeycomb lattice. Two different colors denote the X atoms on the two different planes in the bilayer. In (b), black dotted lines indicate the lateral primitive unit cell. (c) The Brillouin zone of the honeycomb lattice with the reciprocal lattice vectors  $\vec{b}_1$  and  $\vec{b}_2$ .  $\Gamma(0,0,0)$ ,  $K(2\pi/3a, 2\pi/3a, 0)$ , and  $M(\pi/a, 0, 0)$  are the high-symmetry points in the Brillouin zone. Also in (c),  $\bar{\Gamma}$  and  $\bar{K}$  are the high symmetry points in the one-dimensional Brillouin zone for the boundary (edge) along  $\vec{a}$   $(1,0,0)$  direction.

ovskite bilayers and also double-perovskite monolayers in (111) oxide superlattices were investigated and some of them were indeed predicted to host the quantum spin Hall (QSH), QAH and other topological phases (see Refs. [3], [18] and [19] as well as references therein).

In addition, artificial TMO heterostructures nowadays could be prepared with atomic precision, thus providing considerable tunability over fundamental parameters such as SOC, strain and electron correlation. By varying

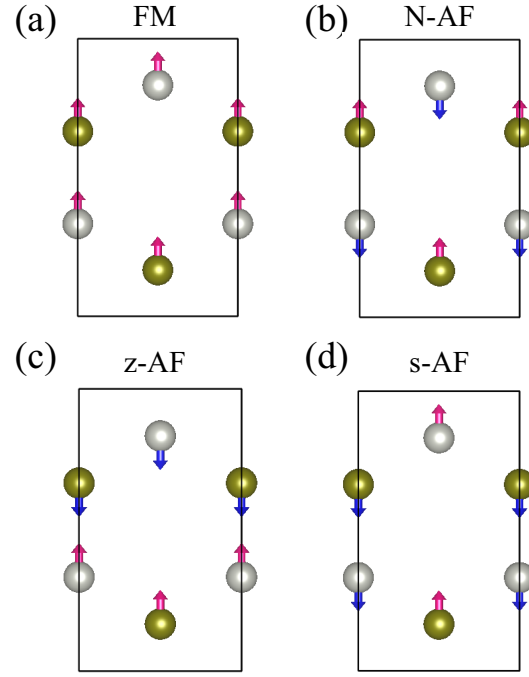


FIG. 2: (a) Ferromagnetic (FM), (b) Néel-antiferromagnetic (AF) (N-AF), (c) zigzag-AF (z-AF) and (d) stripy-AF (s-AF) configurations in the  $(\text{LaXO}_3)_2/(\text{LaO})_{10}$  superlattices. Arrows represent the directions of spin moments on the X atoms.

these fundamental parameters, one could then engineer and also manipulate a number of interesting phenomena such as charge, spin and orbital orderings, metal-insulator transitions, multiferroics and superconductivity in the TMO heterostructures. [13] For example, fascinating phases such as spin-nematic, Dirac half-metallic, QSH, QAH and fully polarized netamtic phases could emerge in (111)  $(\text{LaNiO}_3)_2$  bilayer as the strength of the onsite Coulomb repulsion ( $U$ ) is varied. [20, 21] Moreover, based on his low-energy effective models calculations, Okamoto [22] recently proposed that (111)  $4d$  and  $5d$  TMO perovskite bilayers such as (111)  $(\text{LaPdO}_3)_2$  bilayer where the effects of the SOC and electron correlation are comparable, would provide unique playgrounds for studying quantum phases caused by the interplay of the SOC and electron correlation. Lattice strains can also significantly influence the band structure and electronic properties [15, 23, 24], and are thus another powerful parameter for tuning material properties. Indeed, Liu *et al.* [23] recently showed that topological phase transitions in narrow-gap semiconductors could be engineered by applying strains.

In this paper, we consider (111) bilayers  $(\text{LaXO}_3)_2$  of  $4d$  and  $5d$  transition metal (X) perovskites ( $X = \text{Pd}, \text{Pt}$ ) embeded in an insulating perovskite  $\text{LaAlO}_3$  matrix. In the (111)  $(\text{LaNiO}_3)_2$  bilayer, although the strong onsite correlation could drive it into the QAH phase [20, 21], it remains in the ferromagnetic metallic phase in the realis-

tic  $U$  value range [25] perhaps because of the small SOC on the Ni atoms. Therefore, it would be interesting to see how the electronic properties especially the topology of the band structure would change when the Ni atoms are replaced by the isoelectronic Pd or Pt atoms which have stronger SOC. Furthermore, perovskite  $\text{LaPdO}_3$  [26, 27] has been synthesized and the Pd ion was found to have the same electronic configuration ( $t_{2g}^6 e_g^1$ ) as the Ni ion in perovskite  $\text{LaNiO}_3$ , thus making the fabrication of its (111) heterostructures feasible.

Therefore, here we perform a systematic first-principles DFT study on the magnetic and electronic properties of these (111)  $(\text{LaXO}_3)_2$  bilayers under various biaxial strains as a function of onsite electron correlation. First of all, we find that both bilayers  $(\text{LaXO}_3)_2$  ( $X = \text{Pd}, \text{Pt}$ ) are ferromagnetic with high Curie temperatures. Furthermore, with weak onsite Coulomb repulsion, both systems are Dirac semimetals with Dirac points located slightly above and below the Fermi level. Topologically nontrivial gaps are opened at these Dirac points when the SOC is included. Secondly, bilayer  $(\text{LaPdO}_3)_2$  [ $(\text{LaPtO}_3)_2$ ] becomes a Chern insulator with Chern number  $C = +1$  when the  $U$  value on Pd [Pt] is increased to 3.5 eV [2.0] eV which bring the Dirac points to the Fermi level. Remarkably, bilayer  $(\text{LaPdO}_3)_2$  [ $(\text{LaPtO}_3)_2$ ] becomes a different Chern insulator with Chern number  $C = -1$  when the  $U$  value on Pd [Pt] is further increased slightly to 3.6 eV [2.5] eV. Interestingly, this shows that the direction of chiral edge current could be switched by tuning the  $U$  value. Thirdly, we uncover that the biaxial strain could also drive bilayers into topological phase transitions and also enlarge the topological band gaps as well as lower the critical  $U$  values for the metal-insulator transitions. For example, the critical  $U$  value for the metal-insulator transition is reduced to 2.8 eV for bilayer  $(\text{LaPdO}_3)_2$  under -3 % strain, and to 1.5 eV for bilayer  $(\text{LaPtO}_3)_2$  under -3.5 % strain. Finally the topological band gap in bilayer  $(\text{LaPtO}_3)_2$  could reach as large as 150 meV which is well above room temperature. All these interesting findings thus demonstrate that bilayer  $(\text{LaPdO}_3)_2$  and  $(\text{LaPtO}_3)_2$  are valuable quasi-2D materials for exploring such novel electronic phases as QAH effect at high temperatures and also for technological applications such as low-power consumption nanoelectronics and oxide spintronics.

## II. STRUCTURES AND METHODS

We consider perovskite bilayers  $(\text{LaXO}_3)_2$  sandwiched by an insulating perovskite  $\text{LaAlO}_3$  slab as in the  $(\text{LaXO}_3)_2/(\text{LaAlO}_3)_{10}$  superlattices grown along the [111] direction, where X is either 4d transition metal Pd or 5d transition metal Pt. The resultant superlattices have a trigonal symmetry ( $D_{3d}$ ), and the X atoms in each bilayer form a buckled honeycomb lattice (see Fig. 1). Since the  $\text{LaAlO}_3$  slab is much thicker than the  $(\text{LaXO}_3)_2$  bilayer, the  $\text{LaAlO}_3$  slab could be regarded as the sub-

strate. Therefore, we fix the in-plane lattice constant ( $a$ ) of the superlattices to  $a = \sqrt{2}a_0$ , and  $a_0$  is the theoretical lattice constant of bulk  $\text{LaAlO}_3$  perovskite. The calculated  $a_0$  is 3.81 Å, being close to the experimental value of 3.79 Å [28]. With lattice constant  $a$  and symmetry  $D_{3d}$  fixed, the lattice constant  $c$  and the internal coordinates of all the atoms are theoretically optimized. Note that within this  $D_{3d}$  symmetry constraint, the metal atoms in these superlattices could relax only in the [111]-direction (i.e., out-of-plane direction), although the oxygen atoms could move both laterally and vertically.

The electronic and magnetic structure are calculated based on the DFT with the generalized gradient approximation (GGA) in the form of Perdew-Berke-Ernzerhof [29]. The accurate projector augmented wave (PAW) method [30], as implemented in the VASP code [31, 32], is used. The fully relativistic PAW potentials are adopted in order to include the SOC. The valence configurations of La, Al, Pd, Pt and O atoms used in the calculations are  $4p^6 5s^2 6d^1$ ,  $3s^2 3p^1$ ,  $4p^6 4d^9 5s^1$ ,  $5p^6 5d^9 6s^1$ ,  $2s^2 2p^4$ , respectively. A plane wave cutoff energy of 450 eV and the total energy convergence criteria of  $10^{-5}$  eV are used throughout. A fine Monkhorst-Pack  $k$ -mesh of  $20 \times 20 \times 4$  is used in the selfconsistent calculations.

Because the  $d$ -orbitals of the 4d and 5d transition metal elements are rather extended, the onsite electron-electron repulsion is expected to be moderate but is nonetheless comparable to the strong SOC in these bilayer systems. The interplay of the comparable onsite electron correlation and SOC can lead to such fascinating effects as wide gap Chern Mott insulating phases in (111) 4d and 5d transition metal perovskite bilayers [33] as well as metal-insulator transition, strong topological insulating phase and quantum spin liquid phase in pyrochlore iridates [34–37]. Therefore, in the present calculations, the onsite Coulomb repulsion ( $U$ ) on the Pd and Pt atoms is also taken into account within the GGA +  $U$  scheme [38]. The onsite Coulomb repulsion  $U$  is varied between 0 and 4 eV for Pd and between 0 and 3 eV for Pt.

To understand the magnetic interactions and also to estimate the ferromagnetic ordering temperature ( $T_C$ ) in the bilayers, we consider all possible magnetic configurations in the supercell containing two chemical formula units (see Fig. 2), namely, the FM, Néel-antiferromagnetic (N-AF), zigzag-antiferromagnetic (z-AF) and stripy-antiferromagnetic (s-AF) structures. To evaluate the first-neighbor ( $J_1$ ) and second-neighbor ( $J_2$ ) exchange coupling parameters [see Fig. 1(b)], the calculated total energies of the FM, N-AF and z-AF magnetic configurations are mapped to the classical Heisenberg model  $H = E_0 - \sum_{i>j} J_{ij}(\hat{e}_i \cdot \hat{e}_j)$  where  $J_{ij}$  is the exchange coupling parameter between sites  $i$  and  $j$ , and  $\hat{e}_{i(j)}$  denotes the direction of spin on site  $i(j)$ . This results in  $J_1 = (E_{N-AF} - E_{FM})/12$  and  $J_2 = (E_{z-AF} - E_{FM} - 4J_1)/12$ .

The anomalous Hall conductivity (AHC) for all the ferromagnetic superlattices is calculated based on the Berry-phase formalism [39]. Within this Berry-phase for-

TABLE I: The total energy ( $E$ ) (relative to that of the FM state) and total spin magnetic moment ( $m_s^t$ ) as well as atomic spin magnetic moments of the X atoms ( $m_s^X$ ) and the O atoms ( $m_s^O$ ) that connect two adjacent X atoms in the central layer [Fig. 1(a)] of the converged magnetic configurations (Fig. 2) in the  $(\text{LaXO}_3)_2$  bilayers calculated with  $U = 4$  eV for Pd and  $U = 3$  eV for Pt. Note that the initial N-AF magnetic structure always relaxes to the NM state and thus is not listed here. Also, the initial s-AF magnetic configuration converges to the s-FM state, as listed below.

		FM	NM	z-AF	s-FM
$(\text{LaPdO}_3)_2$	$E$ (meV/cell)	0.0	355.8	106.2	86.2
	$m_s^t$ ( $\mu_B$ /cell)	2.0	0.0	0.0	0.98
	$m_s^{Pd}$ ( $\mu_B$ /atom)	0.81	0.0	0.70	0.79
		0.81	0.0	-0.70	0.04
	$m_s^O$ ( $\mu_B$ /atom)	-0.034	0.0	-0.044	-0.024
$(\text{LaPtO}_3)_2$	$E$ (meV/cell)	0.0	337.0	103.7	83.4
	$m_s^t$ ( $\mu_B$ )	2.0	0.0	0.0	1.0
	$m_s^{Pd}$ ( $\mu_B$ /atom)	0.83	0.0	0.69	0.78
		0.83	0.0	-0.69	0.06
	$m_s^O$ ( $\mu_B$ /atom)	-0.015	0.0	-0.022	-0.013

malism, the AHC ( $\sigma_{ij}^A = J_i^c/E_j$ ) is given as a BZ integration of the Berry curvature for all the valence bands,

$$\sigma_{xy}^A = -\frac{e^2}{h} \sum_{n \in VB} \int_{BZ} \frac{d\mathbf{k}}{(2\pi)^3} \Omega_{xy}^n(\mathbf{k}), \quad (1)$$

$$\Omega_{xy}^n(\mathbf{k}) = - \sum_{n' \neq n} \frac{2Im[p_{ij}^x p_{ji}^y]}{(\epsilon_{\mathbf{k}n} - \epsilon_{\mathbf{k}n'})^2} \quad (2)$$

where  $\Omega_{ij}^n(\mathbf{k})$  is the Berry curvature for the  $n$ th band at  $\mathbf{k}$ .  $J_i^c$  is the  $i$ -component of the charge current density  $\mathbf{J}^c$  and  $E_j$  is the  $j$ -component of the electric field  $\mathbf{E}$ . Since a large number of  $k$ -points are needed to get accurate AHCs, we use the efficient Wannier function interpolation method[40, 41] based on maximally localized Wannier functions (MLWFs) [42]. Since the energy bands around the Fermi level are dominated by X  $e_g$ -orbitals, eight MLWFs per bilayer of X  $e_g$  ( $d^\uparrow, d^\downarrow$ ) orbitals are constructed by fitting to the relativistic band structure in the energy window from -1.5 eV to 1.7 eV for the  $(\text{LaPdO}_3)_2$  bilayer and from -1.5 eV to 0.6 eV for the  $(\text{LaPtO}_3)_2$  bilayer. The band structure obtained by the Wannier interpolation agrees well with that from the DFT calculation. The AHC ( $\sigma_{xy}^A$ ) for both bilayers was then evaluated by taking a very dense  $k$ -point mesh of  $300 \times 300 \times 10$  in the Brillouin zone.

TABLE II: The exchange coupling parameters ( $J_1$  and  $J_2$ ) (see Fig. 1), X magnetic moment in the FM state, Curie temperature ( $T_C$ ), band gap ( $E_g$ ) and Chern number ( $C$ ) of bilayers  $(\text{LaXO}_3)_2$  calculated using different  $U$  values.

$(\text{LaPdO}_3)_2$	$U$ (eV)	0.0	2.0	3.0	3.5	4.0
	$J_1$ (meV)	3.8	14.0	22.3	28.9	35.3
	$J_2$ (meV)	2.57	2.67	3.76	3.94	4.46
	$m_s^{Pd}$ ( $\mu_B$ )	0.35	0.61	0.74	0.78	0.81
	$T_C$ (K)	104	224	346	426	513
	$E_g$ (meV)	0	0	0	4	50
	$C$	-	-	-	1	-1
$(\text{LaPtO}_3)_2$	$U$ (eV)	0.0	1.0	2.0	2.3	3.0
	$J_1$ (meV)	7.1	17.5	32.0	37.6	50.7
	$J_2$ (meV)	2.63	0.87	0.59	0.30	0.29
	$m_s^{Pt}$ ( $\mu_B$ )	0.45	0.60	0.75	0.78	0.83
	$T_C$ (K)	144	223	385	443	595
	$E_g$ (meV)	0	0	8	16	150
	$C$	-	-	1	1	-1

### III. RESULTS AND DISCUSSION

#### A. Magnetic structure

As mentioned above, we perform selfconsistent spin-polarized band structure calculations for the FM, N-AF, z-AF and s-AF magnetic configurations (Fig. 2) in the  $(\text{LaXO}_3)_2$  bilayers. Nonetheless, we find that the initial N-AF magnetic configuration always converges to the nonmagnetic (NM) state, i.e., the metastable N-AF magnetic configuration does not exist in these systems. Interestingly, the initial s-AF magnetic configuration relaxes to a stripy-ferromagnetic (s-FM) configuration with different magnetic moments on the X atoms (Table I). The principal properties of all the converged magnetic configurations obtained with  $U = 4$  eV for Pd and  $U = 3$  eV for Pt are listed in Table I, as examples. As Table I shows, the FM state has the lowest total energy and hence is the ground state magnetic structure. The s-FM configuration has a higher total energy than the FM state but is lower in total energy than the z-AF configuration. The NM state has the largest total energy. For  $U = 4$  (3) eV, the calculated magnetic moment on Pd (Pt) in the  $(\text{LaPdO}_3)_2$  [ $(\text{LaPtO}_3)_2$ ] bilayer is 0.81 (0.83)  $\mu_B$ /atom in the FM state,  $\pm 0.70$  ( $\pm 0.69$ )  $\mu_B$  in the z-AF state, and 0.79/0.04 (0.78/0.06)  $\mu_B$  in the s-FM state (see Table I). Interestingly, the magnetic moment of the O atom connecting the two adjacent Pd (Pt) atoms has a spin polarization being opposite to that of Pd (Pt) in the FM configuration. For example, the O magnetic moment is -0.034  $\mu_B$  and the Pd magnetic moment is 0.81  $\mu_B$  in the  $(\text{LaPdO}_3)_2$  bilayer at  $U = 4$  eV. The opposite spin polarizations of the O and Pd (Pt) atoms is due to the hybridization of the Pd (Pt)  $d$  and O  $p$  orbitals in the FM state.

As described in the preceeding section, the exchange coupling parameters  $J_1$  and  $J_2$  could be evaluated once the total energies of the FM, N-AF and z-AF magnetic

configurations are known. However, as mentioned above, the metastable N-AF state does not exist in these bilayer systems. Therefore, we perform further constrained DFT calculations for the N-AF magnetic configuration for both bilayer structures. Using the total energies from these constrained DFT calculations, we derive the nearest-neighbor and second-neighbor magnetic coupling parameters between the X atoms in the  $(\text{LaXO}_3)_2$  bilayers, as listed in Table II. All the calculated exchange coupling parameters are positive and thus the magnetic interaction between the X atoms is ferromagnetic. In both systems,  $J_1$  is larger than  $J_2$  and increases rapidly with the  $U$  value. In the present Heisenberg model (see Sec. II), the square of the local magnetic moment size has been incorporated into the exchange coupling parameters ( $J$ s). Thus, the rapid increase in the  $J_1$  value with  $U$ , largely reflects the enhanced X magnetic moment due to the stronger onsite Coulomb repulsion  $U$  (see Table II), although the intrinsic first near-neighbor FM coupling  $[J_1/(m_s^X)^2]$  does increase gradually as the  $U$  increases. In contrast,  $J_2$  decreases with the  $U$  value in the  $(\text{LaPtO}_3)_2$  bilayer while it increases slightly in the  $(\text{LaPdO}_3)_2$  bilayer. In the mean-field approximation,  $k_B T_C = \frac{1}{3} \sum z_i J_i$  where  $z_i$  is the number of the  $J_i$  X-X bonds for an X atom. Thus, we could roughly estimate magnetic ordering temperature  $T_C$  using the calculated  $J_1$  and  $J_2$  values. Table II indicates that the estimated Curie temperatures  $T_C$  increases from  $\sim 100$  K to that ( $\sim 500$  K) above room temperature as the  $U$  increases. Note that the Curie temperature given by the mean-field approximation is generally too high by as large as a factor of 2. [43].

## B. Electronic band structure

Let us now examine the main features of the electronic band structures of the  $(\text{LaXO}_3)_2$  bilayers. The band structures calculated without and with the SOC for the FM bilayers with  $U = 4$  eV for Pd and  $U = 3$  eV for Pt are displayed in Fig. 3. In the absence of SOC, both bilayers are half-metallic, with the energy bands in the vicinity of the Fermi level being purely spin-up Pd  $e_g$ -O  $p$  hybridized antibonding bands [see Figs. 3(a) and 3(d)]. This half-metallicity is consistent with the integer value of the total spin magnetic moment ( $2.0 \mu_B/\text{cell}$ ) (Table I). A distinctive set of four bands emerges for each spin channel, namely, rather flat bottom and top bands connected by two dispersive bands in between, which cross at the K and K' points [in the dotted line box labelled 1 in Figs. 3(a) and 3(d)] and thus form two Dirac cones just above the Fermi level, being consistent with the tight-binding model for a honeycomb lattice with a FM open  $e_g$  shell [17]. These Dirac nodal points at the K and K' points are protected by the trigonal symmetry. The band structures presented in Fig. 3 are similar to that of the  $\text{LaNiO}_3$  bilayer [20, 21, 25]. However, the much stronger SOC on the heavier Pd and Pt atoms should have signif-

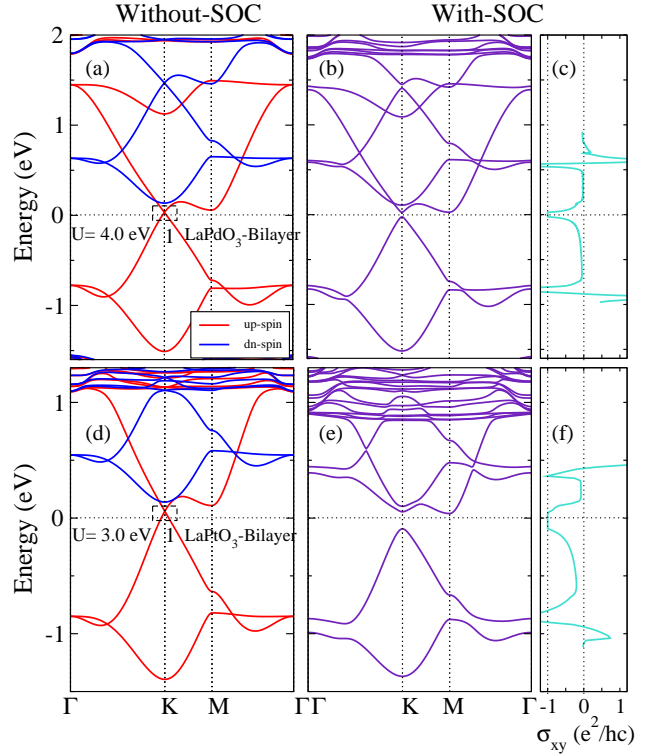


FIG. 3: Band structures without (a,d) and with (b,e) SOC as well as anomalous Hall conductivity ( $\sigma_{xy}$ ) (c,f) of the  $(\text{LaPdO}_3)_2$  (a,b,c) and  $(\text{LaPtO}_3)_2$  (d,e,f) bilayers for  $U = 4$  eV on Pd and  $U = 3$  eV on Pt. Zero refers to the Fermi level.

icant effects on the band structures of these 4d and 5d transition metal perovskite bilayers. Indeed, when the SOC is switched-on, the two spin-up crossing bands (red curves) hybridize and the Dirac points become gapped, resulting in an insulating gap at the Fermi level [Figs. 3(b) and 3(e)]. Both  $(\text{LaPdO}_3)_2$  and  $(\text{LaPtO}_3)_2$  bilayers are, therefore, SOC-driven insulators with the large band gaps of about 50 meV and 150 meV, respectively.

To understand the nature of the lower conduction bands and upper valence bands in a wide energy range, we plot in Fig. 4 the atom-decomposed densities of states (DOS) for bulk  $\text{LaPdO}_3$  and its FM  $(\text{LaPdO}_3)_2$  bilayer. Since the  $(\text{LaPtO}_3)_2$  bilayer exhibits similar features of the valence and conduction bands, here we focus on the electronic structure of bilayer  $(\text{LaPdO}_3)_2$  only. In bulk  $\text{LaPdO}_3$ , the valence bands extending from -7.0 to about -1.2 eV are the strongly Pd  $t_{2g}$  and O  $p$  orbital hybridized bonding bands with the Pd  $t_{2g}^{6\uparrow\downarrow}$  shell fully occupied [Fig. 4(a)]. The lower conduction bands ranging from -0.6 eV to 2.8 eV, on the other hand, consist of the Pd  $e_g$  and O  $p$  orbital hybridized antibonding bands and are partially filled. Thus bulk  $\text{LaPdO}_3$  is predicted to be a NM metal. Experimentally, bulk  $\text{LaPdO}_3$  is found to be a paramagnetic metal [26, 27] and the formal valence of Pd is 3+. This corresponds to a partially filled 4d shell of  $t_{2g}^6 e_g^1$ , i.e., one electron in the doubly degenerate  $e_g$  manifold and six electrons completely filling the  $t_{2g}$  shell. The cal-



culated atom-decomposed DOSs displayed in Fig. 4(a) are consistent with these experimental results.

In the (111)  $(\text{LaPdO}_3)_2/(\text{LaPdO}_3)_{10}$  superlattice, the transition metal perovskite bilayer is sandwiched by a wide-band gap perovskite  $\text{LaAlO}_3$  slab. Thus, the conduction bands made up of transition metal  $d$  orbitals are confined within the bilayer. Consequently, in these superlattices, an important difference is that the eight  $X e_g$ -dominated conduction bands near the Fermi level are narrower. For example, the bandwidth of the spin-down Pd  $e_g$  conduction band gets significantly reduced from about 3.2 eV in bulk  $\text{LaPdO}_3$  to just  $\sim 2.0$  eV in the (111)  $(\text{LaPdO}_3)_2/(\text{LaPdO}_3)_{10}$  superlattice (see Fig. 4). This conduction band narrowing results mainly from two effects, namely, that the hopping within each bilayer must proceed by a repeated 90-deg change in the hopping direction in the cubic lattice and that the X atoms in each bilayer undergo a significant reduction of the coordination number. The significant narrowing of the conduction band leads to enhanced intra-atomic exchange interaction among the  $e_g$  electrons and thus results in the formation of the Pd local spin magnetic moment. The resultant Pd magnetic moments are then coupled ferromagnetically via the nonmagnetic O atom that connects the two neighboring Pd atoms sitting, respectively, in the upper and lower Pd layers [see Figs. 1(a) and 1(b)]. As pointed out by Kanamori and Terakura [44], the spin-up O  $p$  orbitals would hybridize with the spin-up  $e_g$  orbitals of the neighboring Pd atoms and form the Pd  $e_g$  and O  $p$  orbital antibonding conduction bands. Consequently, the spin-up O  $p$  conduction band would be pushed up slightly and this would result in an energy gain by transferring some electrons from the spin-up O  $p$  band to the spin-down O  $p$  band. Thus, the nonmagnetic O atom would become negatively spin-polarized and the small resultant O spin magnetic moment is antiparallel to that of the neighboring Pd atoms (see Table I). The size of this induced O spin magnetic moment would thus reflect the strength of such ferromagnetic coupling between the neighboring Pd atoms. Clearly, this Kanamori and Terakura mechanism would not work if the neighboring Pd atoms are to couple antiferromagnetically, since no induced O magnetization would be possible and hence no energy gain would occur in this case. [44]

### C. Quantum anomalous Hall phases vs. onsite correlation

As mentioned before, the FM  $(\text{LaXO}_3)_2$  bilayers are found to be semiconductors with the insulating gap opened near the Dirac points when the SOC is included. We thus could expect that the band gap would be topologically nontrivial and hence the bilayers could be Chern insulators. To verify the topological nature of these insulating gaps, we calculate the AHC ( $\sigma_{xy}$ ) for these bilayers. For a three-dimensional (3D) quantum Hall insulator,  $\sigma_{xy} = C e^2/hc$  where  $c$  is the lattice constant

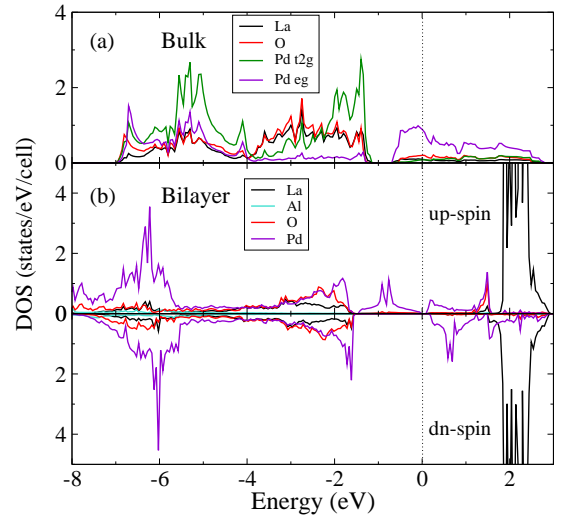


FIG. 4: Atom-decomposed densities of states (DOS) of bulk  $\text{LaPdO}_3$  and its FM  $(\text{LaPdO}_3)_2$  bilayer calculated with SOC and  $U = 4$  eV.

along the  $c$ -axis normal to the plane of longitudinal and Hall currents and  $C$  is an integer known as the Chern number [45]. For a normal FM insulator, on the other hand,  $\sigma_{xy} = 0$ . The calculated AHC of the  $(\text{LaXO}_3)_2$  bilayers is displayed in Fig. 3 for  $U = 4$  eV on Pd and  $U = 3$  eV on Pt. Indeed, Figs. 3(c) and 3(f) show that in both FM  $(\text{LaXO}_3)_2$  bilayers,  $\sigma_{xy} = -1 e^2/hc$  in the gap regions. This demonstrates that both bilayers are QAH insulators with Chern number  $C = -1$ .

To see how the band structure and topological phase change when the strength of onsite Coulomb repulsion  $U$  is varied, we plot in Figure 5 the band structures calculated without and with the SOC for  $U = 3.5$  eV on Pd and  $U = 2.3$  eV on Pt. Interestingly, the spin-up and spin-down  $X e_g$  dominant bands in the bilayers now cross each other at the Fermi energy, resulting in that the two bilayers are a metal [Figs. 5(a) and 5(d)]. Compared with the band structure with a larger  $U$  value on Pd and Pt [Figs. 3(a) and 3(d)], the spin-down bands move slightly downward because of the smaller X magnetic moments (see Table II) and thus the smaller exchange splitting of the spin-up and spin-down  $e_g$  dominant bands. When the SOC is switched-on, these crossing points become gapped with a global band gap of  $\sim 4.0$  meV in the  $(\text{LaPdO}_3)_2$  bilayer and of  $\sim 16.0$  meV in the  $(\text{LaPtO}_3)_2$  bilayer [see the enlarged view around the K point in the inset in Figs. 5(b) and 5(e), respectively]. The band structures of this kind are similar to that of the graphene-based heterostructure [46–48], in which a band inversion between two  $\pi$  bands is induced by the SOC and this band inversion results in a nontrivial band topology. In fact, the band gaps between the different spin-polarized  $X e_g$  bands in the  $(\text{LaXO}_3)_2$  bilayers here [Figs. 5(b) and 5(e)] are also topologically nontrivial. Indeed, Figs. 5(c) and 5(f) show that the calculated  $\sigma_{xy} = +1 e^2/hc$  within the gap, indicating that both bilayers are Chern insulators

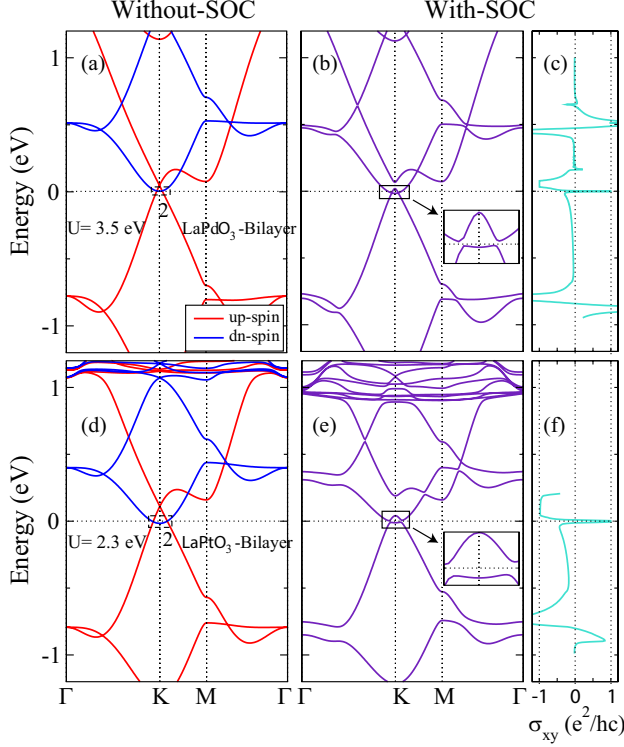


FIG. 5: Band structures without (a,d) and with (b,e) SOC as well as anomalous Hall conductivity ( $\sigma_{xy}$ ) (c,f) of the (LaPdO<sub>3</sub>)<sub>2</sub> (a,b,c) and (LaPtO<sub>3</sub>)<sub>2</sub> (d,e,f) bilayers for  $U = 3.5$  eV on Pd and  $U = 2.3$  eV on Pt. Zero refers to the Fermi level.

with Chern number  $C = +1$ . Interestingly, the Dirac points of the spin-up bands at the K point mentioned above, now move above the Fermi level [Figs. 5(a) and 5(d)]. They become gapped when the SOC is included [see Figs. 5(b) and 5(e)]. For the sake of clarity, let us call the gaps of this kind the local gaps. The global band gaps calculated with the SOC included for different  $U$  values are listed in Table II. It should be noted that this SOC-induced global band gap disappears when  $U$  is less than 3.5 eV in the (LaPdO<sub>3</sub>)<sub>2</sub> bilayer and 2.0 eV in the (LaPtO<sub>3</sub>)<sub>2</sub> bilayer. Nonetheless, the nontrivial local band gaps remain open as long as the SOC is tuned on (see the Appendix).

Interestingly, the sign of  $\sigma_{xy}$  (Chern number) changes from  $-1 e^2/hc$  ( $-1$ ) to  $+1 e^2/hc$  ( $+1$ ) when the onsite Coulomb repulsion is lowered from 4.0 (3.0) eV to 3.0 (2.3) eV for Pd (Pt) in the (LaPdO<sub>3</sub>)<sub>2</sub> [(LaPtO<sub>3</sub>)<sub>2</sub>] bilayer. This implies that the direction of the chiral edge current would be reversed by the change of the onsite correlation strength. The enlarged energy bands near the Fermi level and gap Berry curvature along the high symmetry lines are displayed in Fig. 6 for the (LaPdO<sub>3</sub>)<sub>2</sub> bilayer with  $U = 3.5$  and 4.0 eV for Pd. The gap Berry curvature distributions on the  $k_z = 0$  plane are also shown in the insets in Figs. 6(b) and 6(d). One clearly sees the pronounced peaks in the vicinity of the K points with

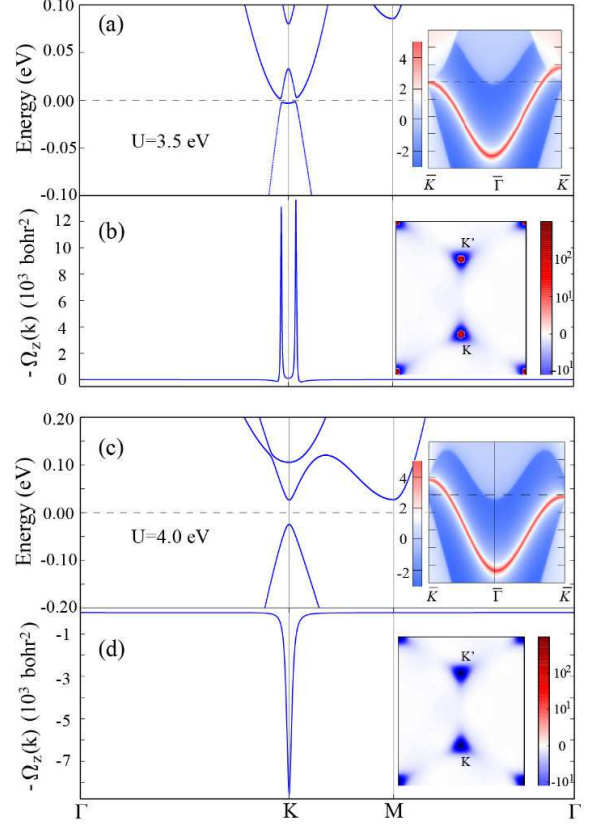


FIG. 6: Energy bands (a,c) and Berry curvature (b,d) along the symmetry lines in the  $k_z = 0$  2D Brillouin zone for the (LaPdO<sub>3</sub>)<sub>2</sub> bilayer. The edge band diagrams are given in the insets in (a,c), and Berry curvature distributions on the  $k_z = 0$  plane in the Brillouin zone are displayed in the insets in (b,d).

different signs for the different  $U$  cases. The calculated edge band diagrams are plotted as spectral functions in Figs. 6(a) and 6(c). In both cases, there is one gapless edge band crossing the Fermi level. Furthermore, the Fermi velocities have opposite signs in these two cases. Therefore, as dictated by the bulk-edge correspondence theorem, the observed one metallic edge state is consistent with Chern number  $|C| = 1$  and also the chirality of the edge state (i.e., the direction of the edge current) conforms with the sign of the Chern number (see Table II). This finding would suggest the possibility of not only achieving the QAH phase but also designing the flow direction of the dissipationless edge current in the FM (LaXO<sub>3</sub>)<sub>2</sub> bilayers by varying the  $U$  value.

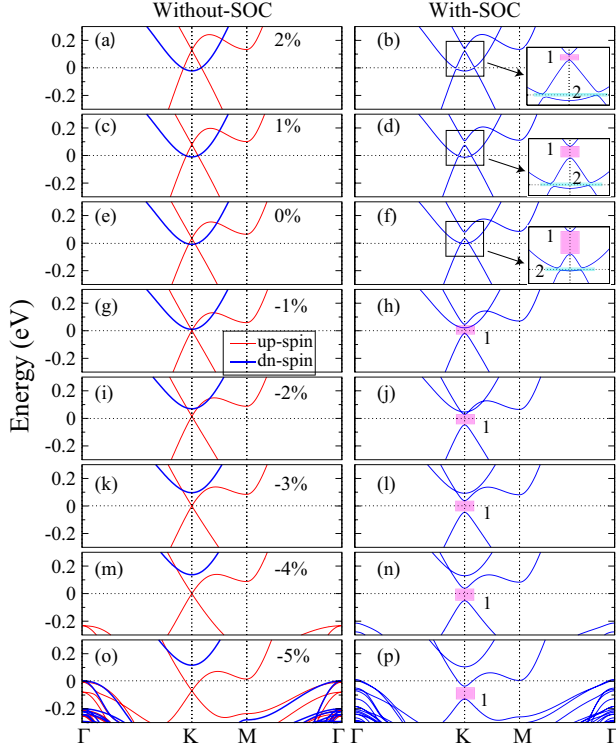


FIG. 7: The band structures calculated without (left panels) and with (right panels) SOC of the  $(\text{LaPdO}_3)_2$  bilayer under various in-plane strains. The  $U = 3.5$  eV is used for Pd. In the left panels, spin-up and spin-down bands are plotted as red and blue curves, respectively. In the right panels, the band gap between two same (opposite) spin bands is labelled as local gap 1 (2). The Fermi level is at 0 eV.

#### D. Strain-driven topological phase transitions

Lattice strains can significantly influence the band structure and electronic properties [23, 24] and are thus an useful parameter for tuning material properties. Therefore, we perform systematic DFT calculations for the  $(\text{LaXO}_3)_2$  bilayers under different in-plane strains ( $\varepsilon$ ). In Fig. 7, we display the energy bands in the vicinity of the Fermi level of the strained FM  $(\text{LaPdO}_3)_2$  bilayer as an example. Interestingly, under a compressive strain, the spin-down band moves upwards steadily as the strain strength increases while the spin-up bands are gradually pushed downwards (see the left panels in Fig. 7). At  $\varepsilon = -1.0$  %, the spin-down band is above the Dirac point of the spin-up bands. In the meantime, the spin-up Dirac point is now close to the Fermi level and remains so for the compressive strain ranging from -1.0 % to -4.0 %. At first glance, such movements of the energy bands caused by the compressive strain seem to be similar to that due to the increased onsite Coulomb repulsion  $U$  which enhances the intraatomic magnetization and hence the exchange band splitting, as described in Sec. III.B. Nonetheless, a close look suggests otherwise.

For example, the calculated X spin magnetic moment hardly changes with the in-plane strain (see Fig. 8). Instead, the size of the mediating O spin magnetic moment increases significantly when the strain is increased. For example, the O spin moment in the  $(\text{LaPdO}_3)_2$  bilayer with  $U = 3.5$  eV for Pd is enhanced from  $-0.034 \mu_B$  in the absence of the strain to  $-0.068 \mu_B$  at  $\varepsilon = -4.0$  %. Since the size of the O spin moment reflects the strength of the FM coupling between the neighboring X atoms, as mentioned before, the compressive strain-enhanced band spin splitting should result from the enhanced interatomic FM coupling caused by the stronger X  $d$  and O  $p$  orbital hybridization due to the shortened X-O bondlengths in the strained  $(\text{LaXO}_3)_2$  bilayers.

When the SOC is included, these Dirac-like band crossing points become gapped, as shown in the right panels in Fig. 7. We can classify these local band gaps into two types, namely, local gap 1 for the gap between the bands of the same spin and local gap 2 for the gap between the bands of the opposite spins. Interestingly, these two types of local band gaps can occur simultaneously in the  $(\text{LaPdO}_3)_2$  bilayer under various tensile strain amplitudes (Figs. 7 and 8). However, local gap 2 disappears in the presence of the compressive strain, while local gap 1 survives all strains although its energy position varies with the in-plane strain size. Importantly, this demonstrates that the band gaps and related electronic properties of the  $(\text{LaXO}_3)_2$  bilayers can be significantly tuned by the in-plane strain.

Let us now summarize the interesting effects of strains on the properties of both  $(\text{LaXO}_3)_2$  bilayers as the strain phase diagrams in Fig. 8. Clearly, compressive in-plane strains increase local gap 1 but suppress local gap 2. However, both local gaps 1 and 2 coexist in the presence of tensile strains, although local gap 2 is much smaller than local gap 1. Remarkably, both local gaps are topologically nontrivial with their Chern numbers having opposite signs, namely,  $C = -1$  for local gap 2 and  $C = +1$  for local gap 1. Meanwhile, the global band gap in the presence of tensile strains is determined by local gap 2 while it originates from local gap 1 in the presence of compressive strains. Consequently, although both bilayers are QAH insulators under both types of strains, their topological phase changes from  $C = +1$  in the tensile strain regime to  $C = +1$  in the compressive strain regime. This interesting finding suggests that both  $(\text{LaXO}_3)_2$  bilayers would offer a rich playground for topological transport studies. Moreover, Fig. 8 shows that the global band gap can reach up to 92 meV in bilayer  $(\text{LaPdO}_3)_2$  under a 4 % in-plane compression and to 242 meV in bilayer  $(\text{LaPtO}_3)_2$  when a 5% in-plane compression is applied. All these results thus indicate that tunable high temperature QAH phase could be realized in bilayers  $(\text{LaXO}_3)_2$  by adjusting the in-plane strain.

Finally, we note that compared to the QAH phases predicted so far in other real materials [3], the QAH phases in bilayer  $(\text{LaXO}_3)_2$  (X = Pd, Pt) have, at least, one distinct feature, i.e., the topological band gaps can be opened



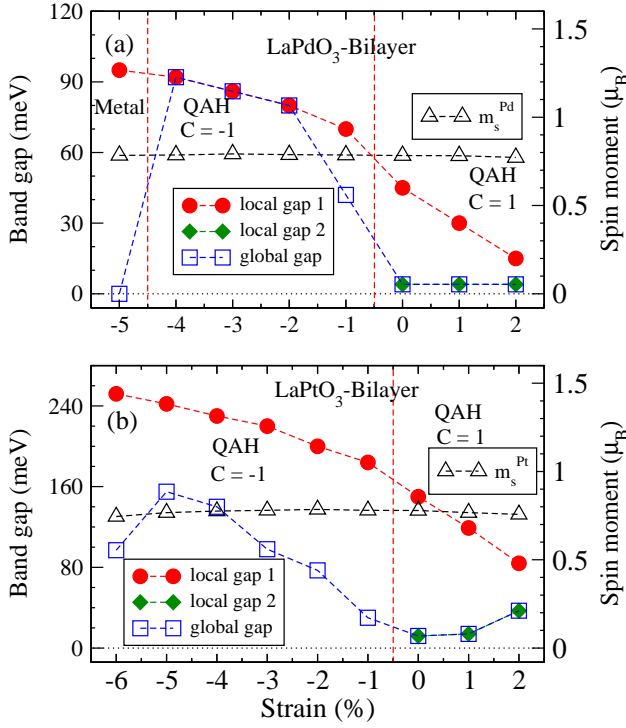


FIG. 8: Calculated global gap, type 1 local gap, type 2 local gap and also X spin moment ( $m_s^X$ ) in the FM  $(\text{LaXO}_3)_2$  bilayers as a function of the biaxial in-plane strain with  $U = 3.5$  (2.3) eV for Pd (Pt). Red vertical dashed lines denote the phase boundaries.

not only in the crossing bands of the same spin but also in the crossing bands of opposite spins in the same system. Moreover, the direction of the dissipationless edge current can be switched by either the onsite Coulomb repulsion  $U$  or in-plane strain  $\varepsilon$ . This is similar to the cases considered previously [49], in which the QAH gaps can be manipulated by the external electric fields. Therefore, the QAHE predicted here in bilayers  $(\text{LaXO}_3)_2$  ( $X = \text{Pd}, \text{Pt}$ ) would be superior for low-power consumption nanoelectronic and spintronic applications.

#### IV. CONCLUSIONS

In summary, we have performed a systematic first-principles DFT study of the magnetic and electronic properties of perovskite bilayers  $\text{LaXO}_3$  ( $X = \text{Pd}, \text{Pt}$ ) imbedded in the (111)  $(\text{LaXO}_3)_2/(\text{LaAlO}_3)_{10}$  superlattices. Interestingly, we find that these TMO perovskite bilayers are high Curie temperature ferromagnets that would host both QAH and Dirac semimetal (see Fig. 9 in the Appendix) phases. Remarkably, in the QAH phase both the direction (the sign of Chern number) and spin-polarization of the chiral edge currents are tunable by either onsite electron correlation or biaxial in-plane strain. Furthermore, the nontrivial band gap can be enhanced up to 92 meV in the  $\text{LaPdO}_3$  bilayer by the compressive

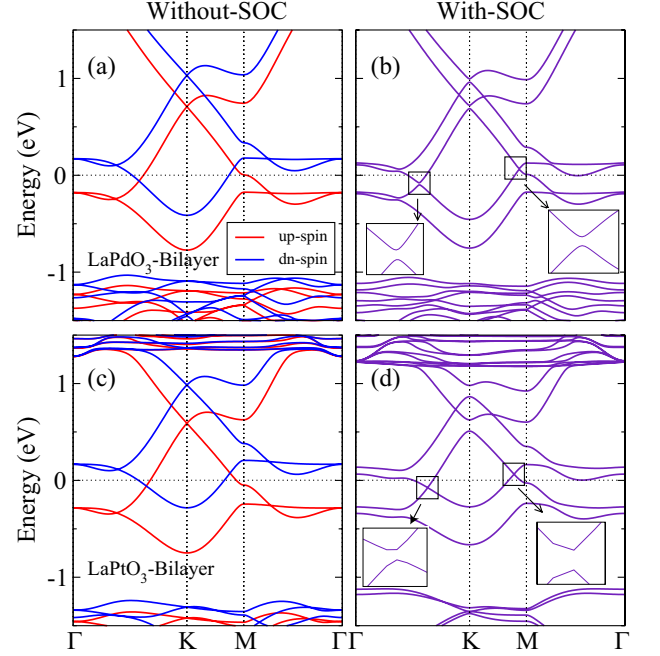


FIG. 9: Band structures without (a,c) and with (b,d) SOC of the  $(\text{LaPdO}_3)_2$  (a,b) and  $(\text{LaPtO}_3)_2$  (c,d) bilayers from the GGA calculations. Zero refers to the Fermi level.

in-plane strain, and can go up to as large as 242 meV when the Pd atoms are replaced by the heavier Pt atoms. By analyzing their underlying electronic band structures, we also uncover the microscopic mechanisms of the FM coupling and other interesting properties of the bilayers. Our findings thus show that (111) perovskite  $\text{LaXO}_3$  ( $X = \text{Pd}, \text{Pt}$ ) (111) bilayers are quasi-2D high temperature FM insulators for investigating exotic quantum phases tunable by both onsite electron correlation and biaxial in-plane strain, and also for advanced applications such as low-power nanoelectronics and oxide spintronics.

#### Acknowledgments

The authors acknowledge the supports from the Ministry of Science and Technology, National Center for Theoretical Sciences, and Academia Sinica of the Republic of China. H. L. is also supported by the National Natural Science Foundation of China under Grants No.11704046.

#### APPENDIX: The GGA band structures

The band structures of the  $(\text{LaPdO}_3)_2$  and  $(\text{LaPtO}_3)_2$  bilayers from the GGA calculations are displayed in Fig. 9. As one can see from Figs. 9(a) and 9(c), in the absence of SOC, there are two Dirac points near the Fermi level, one slightly below the Fermi level along the  $\Gamma$ -K symmetry line and the other slightly above the Fermi level along the K-M line. Therefore, both systems are a Dirac

semimetal. When the SOC is included, type 2 local gaps of 21 and 12 meV open at the Dirac points in bilayer  $(\text{LaPdO}_3)_2$  [see Fig. 9(b)] and local gaps of 7 and 3 meV open in bilayer  $(\text{LaPtO}_3)_2$  [Fig. 9(d)]. Nonetheless, both systems are still Dirac semimetals with their Fermi level

cutting through the two Dirac cones below and above the Dirac points, respectively. Furthermore, type 1 local gaps of 36 [116] meV open at the Dirac points at the K point significantly above the Fermi level in bilayer  $(\text{LaPdO}_3)_2$   $[(\text{LaPtO}_3)_2]$ .

- 
- [1] M. Z. Hasan and C. L. Kane, *Rev. Mod. Phys.* **82**, 3045 (2010).
- [2] X.-L. Qi and S.-C. Zhang, *Rev. Mod. Phys.* **83**, 1057 (2011).
- [3] H. M. Weng, R. Yu, X. Hu, X. Dai, and Z. Fang, *Advances in Physics*, **64**, 227 (2015).
- [4] F. D. M. Haldane, *Phys. Rev. Lett.* **61**, 2015 (1988).
- [5] C. X. Liu, X.-L. Qi, X. Dai, Z. Fang and S.-C. Zhang, *Phys. Rev. Lett.* **101**, 146802 (2008).
- [6] R. Yu, W. Zhang, H. J. Zhang, S. C. Zhang, X. Dai, and Z. Fang, *Science* **329**, 61 (2010).
- [7] Z. H. Qiao, S. A. Yang, W. X. Feng, W.-K. Tse, J. Ding, Y. G. Yao, J. Wang and Q. Niu, *Phys. Rev. B* **82**, 161414(R) (2010).
- [8] T.-W. Chen, Z.-R. Xiao, D.-W. Chiou and G. Y. Guo, *Phys. Rev. B* **84**, 165453 (2011).
- [9] J. Zhou, Q.-F. Liang, H. Weng, Y. B. Chen, S.-H. Yao, Y.-F. Chen, J. Dong and G. Y. Guo *Phys. Rev. Lett.* **116**, 256601(2016).
- [10] C.-Z. Chang, J. Zhang, X. Feng, J. Shen, Z. Zhang, M. Guo, K. Li, Y. Ou, P. Wei, L.-L. Wang, Z.-Q. Ji, Y. Feng, S. Ji, X. Chen, J. Jia, X. Dai, Z. Fang, S.-C. Zhang, K. He, Y. Wang, L. Lu, X.-C. Ma, Q.-K. Xue, *Science* **340**, 167 (2013).
- [11] K.-I. Kobayashi, T. Kimura, H. Sawada, K. Terakura and Y. Tokura, *Nature (London)* **295**, 794 (1998).
- [12] J. Mannhart and D. G. Schlom, *Science* **327**, 1607 (2010).
- [13] H. Y. Hwang, Y. Iwasa, M. Kawasaki, B. Keimer, N. Nagaosa and Y. Tokura, *Nature Mater.* **11**, 103 (2012).
- [14] A. Ohtomo and H. Y. Hwang, *Nature* **427**, 423 (2004).
- [15] P.-W. Lee, V. N. Singh, G. Y. Guo, H.-J. Liu, J.-C. Lin, Y.-H. Chu, C. H. Chen and M.-W. Chu, *Nature Comms.* **7**, 12773 (2016).
- [16] H.-S. Lu, T.-Y. Cai, S. Ju, and C.-D. Gong, *Phys. Rev. Applied* **3**, 034011 (2015).
- [17] D. Xiao, W. Zhu, Y. Ran, N. Nagaosa, and S. Okamoto, *Nature Comms.* **2**, 596 (2011).
- [18] H. K. Chandra, and G. Y. Guo, *Phys. Rev. B* **95**, 134448 (2017).
- [19] S. Okamoto and D. Xiao, *J. Phys. Soc. Jpn.* **87**, 041006 (2018).
- [20] A. Rüegg and G. A. Fiete, *Phys. Rev. B* **84**, 201103(R) (2011).
- [21] K. Y. Yang, W. Zhu, D. Xiao, S. Okamoto, Z. Wang and Y. Ran, *Phys. Rev. B* **84**, 201104(R) (2011).
- [22] S. Okamoto, *Phys. Rev. Lett.* **110**, 066403 (2013).
- [23] J. Liu, Y. Xu, J. Wu, B.-L. Gu, S. B. Zhang and W. Duan, *Acta Cryst. C* **708**, 118 (2014).
- [24] T.-C. Wang, C.-H. Hsu, Z.-Q. Huang, F.-C. Chuang, W.-S. Su and G.-Y. Guo, *Sci. Rep.* **6**, 39083 (2016).
- [25] A. Rüegg, C. Mitra, A. A. Demkov, and G. A. Fiete, *Phys. Rev. B* **85**, 245131 (2012).
- [26] S. J. Kim, S. Lemaux, G. Demazeau, J. Y. Kim, and J. H. Choy, *J. Am. Chem. Soc.* **123**, 10413 (2001).
- [27] S. J. Kim, S. Lemaux, G. Demazeau, J. Y. Kim, and J. H. Choy, *J. Mater. Chem* **12**, 995 (2002).
- [28] S. Geller and V. B. Bala, *Acta Cryst.* **9**, 1019 (1956).
- [29] J. P. Perdew, K. Burke, and M. Ernzerhof, *Phys. Rev. Lett.* **77**, 3865 (1996).
- [30] P. E. Blöchl, *Phys. Rev. B* **50**, 17953 (1994).
- [31] G. Kresse and J. Hafner, *Phys. Rev. B* **47**, 558(1993).
- [32] G. Kresse and J. Furthmüller, *Phys. Rev. B* **54**, 11169 (1996).
- [33] H. Guo, S. Gangopadhyay, O. Köksal, R. Pentcheva and W. Pickett, *NPJ Quant. Mater.* **2**, 4 (2017).
- [34] J.-M. Carter, V. V. Shankar, M. A. Zeb and H.-Y. Kee, *Phys. Rev. B* **85**, 115105 (2012).
- [35] J.-M. Carter, V. V. Shankar and H.-Y. Kee, *Phys. Rev. B* **88**, 035111 (2013).
- [36] Q. Chen, H.-H. Hung, X. Hu and G. A. Fiete, *Phys. Rev. B* **92**, 085145 (2015).
- [37] R. Schaffer, E. K.-H. Lee, B.-J. Yang and Y. B. Kim, *Rep. Prog. Phys.* **79**, 094504 (2016).
- [38] S. L. Dudarew, G. A. Botton, S. Y. Savrasov, C. J. Humphreys and A. P. Sutton, *Phys. Rev. B* **57**, 1505 (1998).
- [39] D. Xiao, M.-C. Chang and Q. Niu, *Rev. Mod. Phys.* **82**, 1959 (2010).
- [40] X. Wang, J. R. Yates, I. Souza, and D. Vanderbilt, *Phys. Rev. B* **74**, 195118 (2006).
- [41] M. G. Lopez, D. Vanderbilt, T. Thonhauser, and I. Souza, *Phys. Rev. B* **85**, 014435 (2012).
- [42] N. Marzari, A. A. Mostofi, J. R. Yates, I. Souza, and D. Vanderbilt, *Rev. Mod. Phys.* **84**, 4 (2012).
- [43] Y. Feng, S. Wu, Z.-Z. Zhu and G.-Y. Guo, *Phys. Rev. B* **98**, 125416 (2018).
- [44] J. Kanamori and K. Terakura, *J. Phys. Soc. Jpn.* **70**, 1433 (2001).
- [45] B. I. Halperin, *Jpn. J. Appl. Phys. Suppl.* **85**, 1913 (1987).
- [46] Z. Qiao, W. Ren, H. Chen, L. Bellaïche, Z. Zhang, A. H. MacDonald, and Q. Niu, *Phys. Rev. Lett.* **112**, 116404 (2014).
- [47] J. Zhang, B. Zhao, Y. Yao, and Z. Yang, *Phys. Rev. B* **92**, 165418 (2015).
- [48] Z. Wang, C. Tang, R. Sachs, Y. Barlas, and J. Shi, *Phys. Rev. Lett.* **114**, 016603(2015).
- [49] H. Zhang, C. Lazo, S. Blügel, S. Heinze, and Y. Mokrousov, *Phys. Rev. Lett.* **108**, 056802(2012).